The Astrophysical Journal Supplement Series, 282:4 (12pp), 2026 January https://doi.org/10.3847/1538-4365/ae1472

Multiscale Magnetic Reconnection in the Genesis of Young Slow Solar Wind

Ziqi Wu[1,2], Jiansen He[1,3], Chuanpeng Hou[4], Die Duan[1], Jia Huang[5], Alexis P. Rouillard[6], Daniel Verscharen[7], Yao Chen[8], Rui Zhuo[1], and Tianhang Chen[1]

[1] School of Earth and Space Sciences, Peking University, Beijing, People's Republic of China; jshept@pku.edu.cn
[2] Center for Mathematical Plasma Astrophysics, KU Leuven, Leuven, Belgium
[3] State Key Laboratory of Solar Activity and Space Weather, National Space Science Center, Chinese Academy of Sciences, Beijing, People's Republic of China
[4] Institut für Physik und Astronomie, Universität Potsdam, Potsdam, Germany
[5] Space Sciences Laboratory, University of California, Berkeley, CA 94720, USA
[6] Institut de Recherche en Astrophysique et Planétologie, Université Toulouse III-Paul Sabatier, CNRS, CNES, France
[7] Mullard Space Science Laboratory, University College London, Dorking, UK
[8] Institute of Space Sciences, Institute of Frontier and Interdisciplinary Science, Shandong University, Weihai, People's Republic of China

Received 2025 August 21; revised 2025 October 14; accepted 2025 October 14; published 2025 December 17

Abstract

The genesis of solar wind remains elusive due to limited multi-instrument observations of its source regions. Here, we introduce a novel "see and touch" technique, integrating remote-sensing observations with in situ measurements from Parker Solar Probe (PSP). This approach allows us to obtain 3D trajectories of flow structures such as streamer blobs and explore their in situ properties. With this approach, we link blobs observed by remote sensing and high-density jets (HDJs) measured in situ. The blobs are embedded in streamer rays, while the HDJs are found when PSP crosses the heliospheric current sheet (HCS). Our findings suggest that large-scale blobs/HDJs originate from primary reconnection in the near-Sun HCS, while secondary reconnection in smaller-scale current sheets forms multiple flux ropes, which merge to trigger further small-scale reconnection. Detailed in situ analysis reveals that turbulent magnetic reconnection is a key mechanism for dissipating filamentary HCS and energizing plasmas in blobs/HDJs. The multiscale magnetic reconnection accelerates the proton core population and mixes it with the beam population, driving bulk acceleration and heating of the nascent slow solar wind.

Unified Astronomy Thesaurus concepts: Solar wind (1534); Heliosphere (711); Solar magnetic reconnection (1504)

Materials only available in the online version of record: animation

1. Introduction

The acceleration and heating mechanisms of the solar wind are important questions in solar physics. It requires not only self-consistent theoretical modeling but also advanced multi-instrument observational approaches (J.-S. He et al. 2008; T. Matsumoto & T. K. Suzuki 2014; S. R. Cranmer et al. 2015; M. Shoda et al. 2019; C. Shi et al. 2022) to solve this long-standing mystery. The solar wind can be divided into the slow solar wind (SSW) and the fast solar wind by speed. The plasma of SSW has properties similar to that of closed-field regions in the solar corona. However, the release and acceleration mechanisms of SSW remain elusive (U. Feldman et al. 2005; L. Abbo et al. 2016). During solar minimum, SSW primarily distributes at low latitudes and is associated with helmet streamers and their heliospheric extensions—the heliospheric current sheet (HCS) and heliospheric plasma sheet (HPS) systems (D. McComas et al. 1998; S. Antiochos et al. 2011; M. J. Owens et al. 2014; P. Riley et al. 2002). Other potential sources of SSW include pseudostreamers, coronal hole boundaries, small coronal holes, and the so-called S-web, where the slow streams are dynamically released through various mechanisms (L. Abbo et al. 2016). Recent results from Parker Solar Probe (PSP) and Solar Orbiter have further advanced our understanding of SSW source regions and acceleration mechanisms, including the role of Alfvénic turbulence and fine-scale jets in coronal holes (D. Telloni et al. 2022; L. P. Chitta et al. 2025).

Observations by white-light heliospheric imagers indicate that bright blobs form at the tips of coronal streamers and flow into the heliosphere quasiperiodically (N. R. Sheeley et al. 1997; Y. M. Wang et al. 1998, 2000; H. Q. Song et al. 2009; N. M. Viall et al. 2021). These blobs are essential components of helmet-streamer-associated SSW. Therefore, investigating the formation of blobs and their impact on the surroundings is critical to understanding the origin and evolution of the SSW. According to observations, streamer blobs are formed at a heliocentric distance of 3–4 $R_\odot$ and have an initial length of 1 $R_\odot$ and a width of 0.1 $R_\odot$. They accelerate from 150 km s^{-1} at 5 $R_\odot$ to 300 km s^{-1} at 25 $R_\odot$ and expand roughly in proportion from 1 to 3 $R_\odot$ in length. Streamer blobs are likely to form by reconnection at the cusp of helmet streamers. Observational evidence includes coronal inflows that occur simultaneously with blob outflows (N. R. J. Sheeley et al. 2001; N. R. J. Sheeley & Y. M. Wang 2014; E. Sanchez-Diaz et al. 2017). Possible candidates for driving the reconnection are intrinsic instabilities of helmet streamers, such as sausage or tearing instabilities (Y. Chen et al. 2009; V. Réville et al. 2022), or the converging flows at the cusp (G. Lapenta & D. A. Knoll 2005).

In situ information on helmet streamers is required to constrain models for streamer blobs. Combining coronagraph images and in situ measurements of HCS and HPS at 1 au, E. Sanchez-Diaz et al. (2019) proposed a model according to which periodical magnetic reconnection creates bands of twisted magnetic field lines attached to the Sun that expand outward in the form of flux ropes; blobs lie in between flux ropes and propagate outward. A. P. Rouillard et al. (2010) identified streamer blobs suppressed by corotation interaction regions in white-light images from STEREO-A and in situ measurements from ACE and STEREO-B at 1 au. PSP's close approach to the Sun provides excellent opportunities to investigate the formation mechanisms, the interior structure, and the boundaries of plasma blobs. During PSP's first orbit, A. P. Rouillard et al. (2020) relate the streamer flows observed by STEREO-A to the density fluctuations measured in situ at 30 $R_{\odot}$; B. Lavraud et al. (2020) identify high-density regions around HCS and HPS, suggesting that the HPS is composed of a succession of high-β blobs. On the other hand, PSP frequently encounters magnetic reconnection exhausts while traversing near-Sun HCS (T. D. Phan et al. 2022; T. Phan et al. 2024). S. Eriksson et al. (2024) identified multiple reconnection exhausts along the HCS observed by PSP using comprehensive in situ analysis and provided precise timing constraints in a Zenodo data repository. Observations suggest that the HPS consists of a series of blobs, which may be related to in situ measured high-density regions. However, it remains to be confirmed whether these blobs and high-density regions are indeed the optical and in situ counterparts of reconnection jet flows within the HCS. Additionally, it is unclear whether blobs are accelerated and heated by reconnection occurring in the HCS. Further investigation is needed to understand the multiscale characteristics and physical processes occurring within blobs and at their boundaries. The role of turbulence in these structures is also yet to be determined. To clarify these points, it is essential to combine remote-sensing and in situ observations more effectively.

This work aims to achieve such a combination based on PSP data by promoting a novel "see and touch" technique. The "seeing" part utilizes remote-sensing observations to provide macroscopic morphologies and the dynamic evolution of streamer structures in background solar wind conditions. We reconstruct the 3D trajectories of streamer blobs according to motion estimation based on monocular image sequence optical flow (MEO-MISOF), a process facilitated by the rapidly changing perspective of PSP during its perihelia passages (P. Liewer et al. 2019; P. C. Liewer et al. 2020, 2022). The "touching" part employs in situ measurements to probe transient flow events, aiming to discern multiscale physics in the transient flow events. The streamer flow structures first seen in white light and later encountered in situ by PSP serve as the targets for "see and touch" analyses.

2. Data and Method

2.1. Data

PSP was launched on 2018 August 12, and has been the closest spacecraft to the Sun ever (N. J. Fox et al. 2016). In this work, we use the measurements in the radial–tangential–normal coordinates from PSP's Encounter 8, including the magnetic field vector ($B_{\rm r}$, $B_{\rm t}$, B_n) measurements from FIELDS (S. D. Bale et al. 2016); proton density (N_p), bulk velocity vector ($V_{\rm r}$, $V_{\rm t}$, $V_{\rm n}$), temperature (T_p), and proton velocity distribution function (VDF) from SWEAP/SPAN-I (J. C. Kasper et al. 2016; R. Livi et al. 2022); and suprathermal electron pitch angle distribution (e-PAD) and electron temperature (T_e) from SWEAP/SPAN-e (P. L. Whittlesey et al. 2020). We also use electron density (N_e) derived by quasi-thermal noise spectroscopy based on data from the Radio Frequency Spectrometer component of the FIELDS suite (M. Pulupa et al. 2017; M. M. Martinović et al. 2022; J. Huang et al. 2023). We use the preprocessed L3 white-light coronal images from WISPR/INNER, in which scattering and ecliptic lights have been removed (A. Vourlidas et al. 2016). Finally, to analyze the positions of the spacecraft and the condition of the cameras, we employ the SPICE data provided by the PSP team (A. Annex et al. 2020). Additionally, we use the Carrington map constructed from STEREO COR2 west-limb images (R. A. Howard et al. 2008) and GONG line-of-sight synoptic maps available at https://gong.nso.edu/.

In this study, we utilize the global magnetohydrodynamic (MHD) simulation data produced by the Magnetohydrodynamic Algorithm outside a Sphere (MAS) model, provided by Predictive Science Inc. (PSI). The MAS model simulates the large-scale solar corona and heliospheric magnetic field structures, which are crucial for interpreting the spacecraft observations within the context of global solar wind and magnetic topology (J. A. Linker et al. 1999; P. Riley et al. 2012). The publicly available MAS datasets were accessed via the PSI website[9] and serve as the basis for visualizing magnetic field lines, the HCS, and flux tube configurations in our analysis.

2.2. See and Touch Technique

We introduce the "see and touch" technique that builds a link between PSP's white-light imaging and in situ measurements. The workflow is outlined in Figure 1. We first identify moving objects in time-differenced WISPR images and J-maps (Figures 1(a)–(b)) as flowing blobs. Then, we employ a 3D motion estimation procedure of these objects based on monocular image sequence optical flow, "MEO-MISOF" (Figures 1(a)–(c)), which is feasible due to the fast-changing perspective of PSP around its perihelia (P. C. Liewer et al. 2020, 2022, 2023). Finally, we compare the reconstructed 3D trajectories of the streamer blobs with PSP's orbit around perihelion and take the streamer flow structures encountered in situ by PSP as targets for "see and touch" studies. These steps are explained in detail in the following sections.

2.2.1. Creating J-maps from WISPR Images

We first obtain running difference images by subtracting image pairs separated by 30 minutes, which reveal moving structures as white–black pairs (N. R. Sheeley et al. 1999) with velocity vectors pointing from the black to the white regions (Figure 1(a)). In WISPR images, the projection of PSP's orbital plane is defined as the line linking the Sun and the intersection between PSP's velocity vector and the image plane. To identify moving structures potentially encountered by PSP, we extract 30 pixel-wide stripes from running difference images along this line and average the brightness to improve the signal-to-noise ratio.

We then construct the J-maps by stacking the extracted stripes in elongation–time coordinates (N. R. Sheeley et al. 1999; N. R. J. Sheeley et al. 2008). The elongation is calculated as the angle between the line of sight (LOS; the line from PSP to the direction specified by a given pixel) and the

---

[9] https://www.predsci.com/

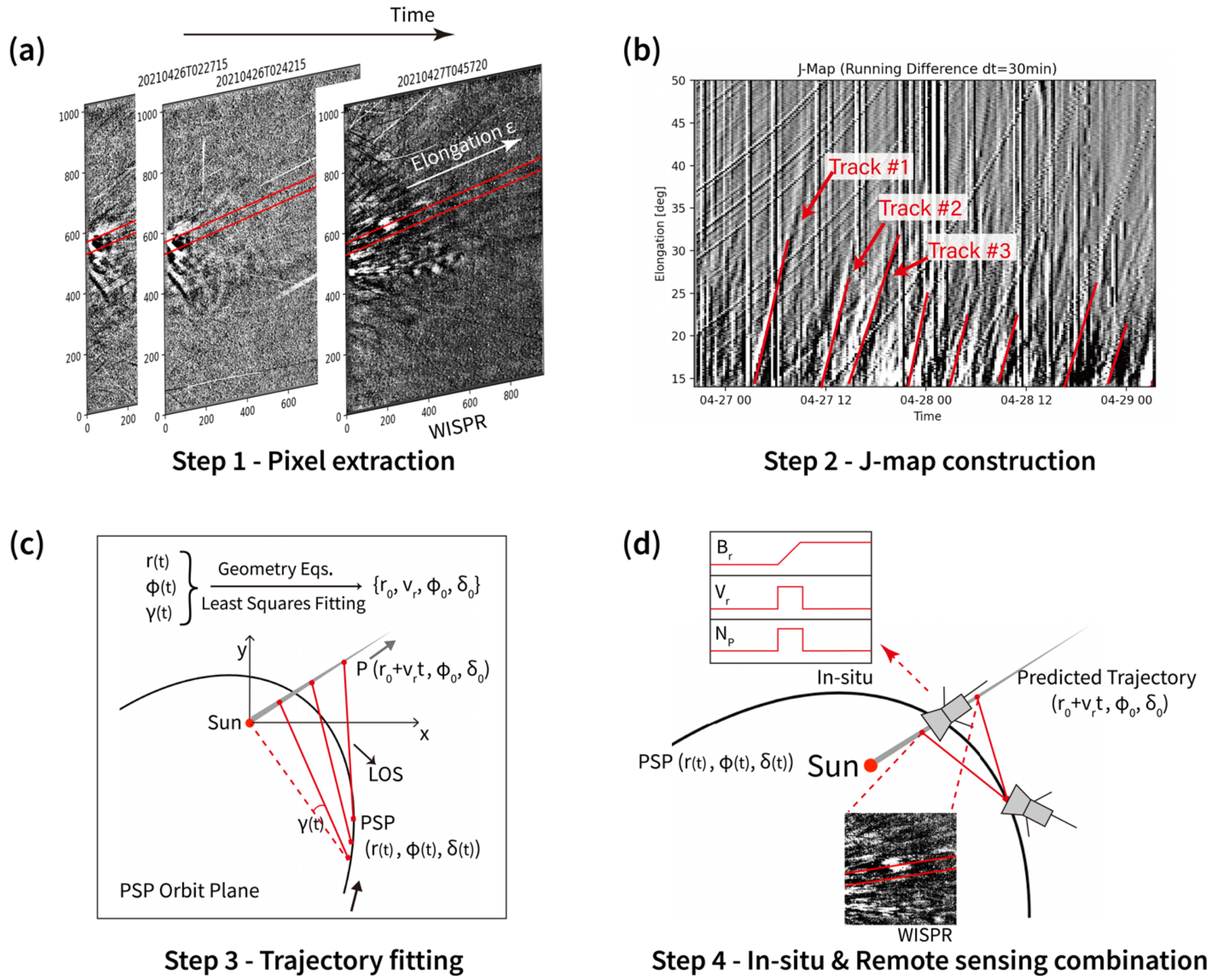

Step 1 - Pixel extraction

Step 2 - J-map construction

Step 3 - Trajectory fitting

Step 4 - In-situ & Remote sensing combination

Figure 1. Workflow of the "see and touch" technique. (a) Extraction of pixels near PSP's orbital plane from a running-difference sequence of WISPR images. (b) Construction of a J-map along PSP's orbital plane to identify outward-propagating structures. (c) Reconstruction of the 3D trajectory of the selected structure under the assumption of constant radial velocity. The gray-shaded ray indicates the structure's path. Solid red lines show the line of sight (LOS) from the structure to PSP, and the corresponding elongation represents its 2D projected position in the image. (d) Comparison between the reconstructed trajectory and PSP's orbit to locate their intersection point along the streamer ray, enabling the alignment of remote-sensing observations with in situ measurements.

PSP–Sun line. Each white–black stripe pair represents a structure moving away from the Sun; steeper slopes indicate higher apparent speed.

Clear and coherent stripes are identified as candidates for further analysis. The supercorotation phase, which occurs approximately 2 days before PSP's perihelion, provides an optimal window for linking remote-sensing observations to in situ measurements. During this phase, PSP's angular velocity exceeds that of the rotating Sun, allowing it to approach corotating structures such as coronal streamers.

2.2.2. Fitting 3D Trajectories of Moving Objects in WISPR's Field of View

Thanks to PSP's fast-moving perspective, we can extract the 3D trajectories of outflowing structures based on their apparent coordinates in a series of WISPR images. The tracking and fitting technique was first proposed by P. C. Liewer et al. (2020); we adopt one-step fitting for structures that move approximately within PSP's orbital plane.

For any target moving in WISPR's field of view, its apparent coordinates can be measured as $(X_{\rm pixel}(t), Y_{\rm pixel}(t))$, which we track and mark manually in WISPR images. The pixel coordinates are then converted to angular coordinates $(\gamma(t), \beta(t))$, where γ represents the in-plane angle (i.e., the angle between the Sun, PSP, and the target's projection onto PSP's orbital plane), and β represents the out-of-plane angle (i.e., the angle between the target, PSP, and its projection onto PSP's orbital plane).

In addition, PSP's heliocentric distances, longitudes, and latitudes in the Heliocentric Inertial (HCI) frame $(r(t), \phi(t), \delta(t))$ are known from its ephemeris data. Assuming the target originates at (r_0, ϕ_0, δ_0) and moves with a constant radial speed $v_{\rm r}$, its trajectory can be described as $(r_0 + v_{\rm r}t, \phi_0, \delta_0)$ in the HCI frame. The four unknown parameters $r_0, v_{\rm r}, \phi_0, \delta_0$ can be determined by fitting the observed $(\gamma(t), \beta(t))$ with the following equations:

$$\frac{\tan\beta(t)}{\sin\gamma(t)} = \frac{\tan\delta_0}{\sin[\phi(t) - \phi_0]}(1 - F\sin\epsilon), \tag{1}$$

$$\cot\gamma(t) = \frac{r(t) - (r_0 + v_{\rm r}t)\cos\delta_0\cos[\phi_0 - \phi(t)]}{(r_0 + v_{\rm r}t)\cos\delta_0\sin[\phi_0 - \phi(t)]} \times (1 - G\sin\delta_0\sin\epsilon), \tag{2}$$

where ϵ is the orbit inclination,

$$F(\phi_0,\ \delta_0,\ \phi(t)) \equiv \frac{\sin\phi_0}{\tan\delta_0} + \frac{\tan\delta_0\cos\phi(t)}{\sin(\phi_0 - \phi(t))} \tag{3}$$

$$\begin{aligned} &G(r_0 + v_\mathrm{r} t,\ \phi_0,\ \delta_0,\ r(t),\ \phi(t)) \\ &\equiv \frac{\sin\phi(t)}{r(t)/(r_0 + v_\mathrm{r} t) - \cos\delta_0\cos(\phi_0 - \phi(t))} \\ &+ \frac{\cos\phi(t)}{\cos\delta_0\sin(\phi_0 - \phi(t))}. \end{aligned} \tag{4}$$

Both Equations (3) and (4) should be used when fitting out-of-plane structures because δ_0 is coupled with other in-plane parameters. In this study, however, we focus on structures near PSP's orbital plane with small δ_0 and β. In these cases, the numerator terms on both sides of Equation (1) approach zero, implying that variations in δ_0 have a negligible influence on ϕ_0. Consequently, Equation (2) independently determines ϕ_0 (P. C. Liewer et al. 2020).

Therefore, we first fit the in-plane parameters r_0, v_r, and ϕ_0 using Equation (2) and then determine δ_0 that yields the least error in $\beta(t)$.

The assumption of a constant radial speed is justified by the expectation that the structures have already reached their terminal velocities. While it is in principle possible to include an acceleration term by introducing an additional parameter a, such that the radial trajectory becomes $(r_0 + v_{r0}t + at^2/2, \phi_0, \delta_0)$, this extension does not yield meaningful improvements in our case, as the inferred acceleration remains negligibly small.

2.2.3. Combining In Situ and Remote Observations

After obtaining the 3D trajectories of structures moving inside PSP's orbital plane, we compare the trajectories with PSP's orbit and find possible spatial conjunctions. PSP crosses specific structures only sporadically. However, PSP often flies across structures with quasi-steady behavior, such as coronal streamers captured by WISPR after or before any transient passes the conjunction. These instances allow us to correlate white-light imaging with in situ measurements at the time of conjunction.

Combining remote observation and in situ measurements allows a multiscale study of the structures. From remote observations, we estimate the size and brightness of the targets and roughly understand their radial evolution on the intermediate scale (around $0.5 \sim 2\ R_\odot$ in size), in addition to the motion parameters obtained from trajectory fitting. In situ measurements, on the other hand, enable us to analyze the magnetic field topology, solar wind properties from large to small scales, and kinetic features in velocity space.

3. Results

3.1. Tracking Blobs in WISPR Images and Reconstructing Their Trajectories

First, we analyze blobs identified in the J-map from 2023 April 27 to 29 (Figure 1(b)). We identify several stripes from the J-map and focus on three clear and coherent tracks (marked as Tracks #1, #2, and #3) for further analysis, because their trajectories potentially intersect with PSP's orbit later around its perihelion, enabling "see and touch" analysis (Figure 2).

For Track #1, Figures 2(a) and (b) show the original and running difference WISPR images. Further examination reveals that this structure consists of two ellipsoid-shaped blobs moving simultaneously, embedded in bifurcated rays. We label them as Tracks #1a and #1b. The 3D trajectory fitting confirms that these rays are nearly in PSP's orbital plane, with blob latitude (i.e., the angle between the track and PSP's orbital plane) being $-0\overset{\circ}{.}035$ for Track #1a and $-0\overset{\circ}{.}09$ for Track #1b. The twin blobs may result from the visual effects of folded HCS or multiple magnetic reconnection events in the HCS.

To obtain the 3D trajectories of the Tracks (#1a, #1b, #2, and #3), we manually mark their positions in a series of images (blue and orange markers in Figures 2(a) and (b)) and perform trajectory fitting based on "MEO-MISOF" using the coordinates of these markers (detailed in Section 2.2.2). For each track, we describe the 3D trajectory as $(r_0 + v_\mathrm{r}t, \phi_0, \delta_0)$ in the HCI frame, where r_0 is the initial radial distance, v_r is the radial speed (assumed to be constant), and ϕ_0 and δ_0 are the initial longitude and latitude. Figure 3 shows detailed trajectory fitting results, including the observed evolution of the in-plane angle $\gamma(t)$ and out-of-plane angle $\beta(t)$, which align with the fitting results. The fitting parameters are shown in Table 1.

We project the predicted tracks (colored lines) onto the J-map to compare with the blob tracks (colored crosses) observed by WISPR (Figure 2(c)), showing that they are in agreement. We also plot the predicted blob positions in Carrington coordinates to compare with PSP's orbit (Figure 2(d)). PSP crosses the trajectories of blobs around April 29. Although the blobs have passed the conjunctions when PSP arrives, we conjecture that PSP still detects substantial information about the physics of these blobs by sampling similar plasma in the following chain of blobs released in the same streamer flow.

The fitting results also reveal that tracks with larger curvatures in the J-map are nearer to the spacecraft due to projection effects, which suggests that the curvature of stripes in the J-map indicates the distance between the outflow structure and PSP (P. Liewer et al. 2019). Track #2, being the most curved in the J-map, is closest to PSP at the imaging time, while Track #3, the straightest, is farthest from PSP at the imaging time.

3.2. Connecting WISPR Images and In Situ Measurements

Figure 4 presents a macroscopic overview of PSP's transition from the periphery to the center of the streamer during Encounter 8. We compare PSP's orbit and the projected positions of blobs in the white-light Carrington map at 13 $R_\odot$, which is constructed from STEREO COR2 west-limb images spanning from April 16 to May 14 (Figure 4(a)) and determine the source regions of the solar wind measured by PSP through two-step ballistic backmapping technique (S. T. Badman et al. 2020; Figure 4(b)). In Figure 4(b), we show the footpoints of PSP on the source surface; there is an offset in Carrington longitude compared to the real orbit shown in Figure 4(a). The whole period can then be divided into one imaging phase and one in situ phase. Figure 5 shows an illustration of PSP's encounter and a combination of observations used in our study; the focused observation at a certain time is highlighted by a green box.

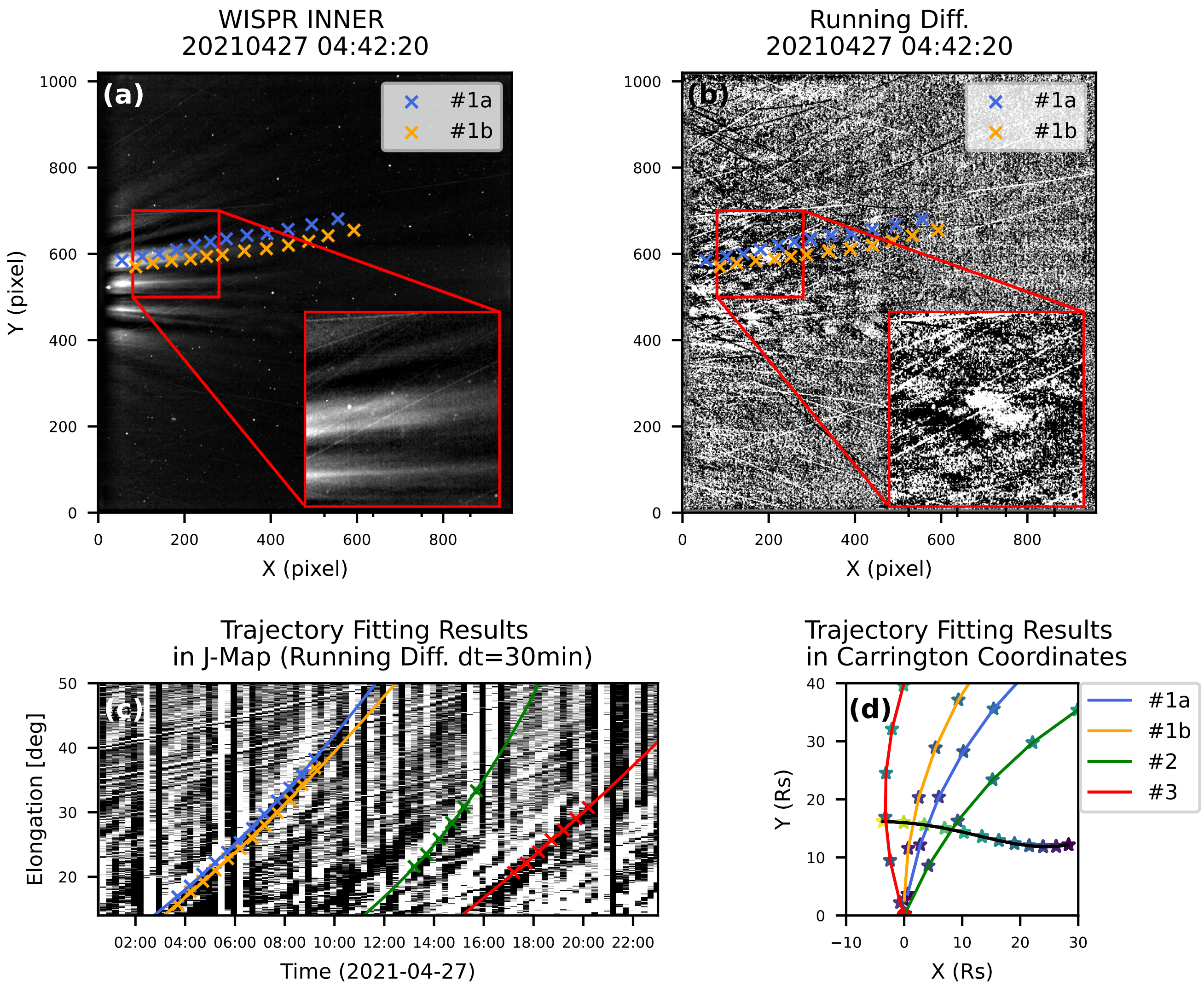

Figure 2. Blobs observed in WISPR and corresponding trajectory fitting results. (a)–(b) Track #1 observed in WISPR images and running-difference images, respectively. Close-up views of the moving structures are shown in the bottom-right corners, highlighting two ellipsoidal blobs, labeled #1a and #1b. Their tracks are indicated by crosses: blue for blob #1a and orange for blob #1b. (c) Trajectory markers (crosses) and the corresponding fitting results (solid lines) projected onto a J-map. (d) The same trajectory fitting results projected in Carrington coordinates. The color scheme is consistent with (c). Star markers, spaced 4 hr apart, indicate the propagation timeline from April 27 to April 30.

For the imaging phase from April 27 00:00 to April 28 13:40, PSP traverses fast, sparse solar wind originating from polar coronal holes, as evidenced by the in situ measurements and source regions (Figures 4(e) and (f)). During this phase, WISPR captures the blobs analyzed in Section 3.1.

For the in situ phase from April 28 13:40 to April 30 00:00, PSP enters slow, dense streamer wind, as indicated by in situ measurements and its projection on the synoptic white-light Carrington map. During this phase, PSP crosses the blobs' paths on April 29 from 00:00 to 12:00.

Consequently, we focus on the in situ measurements at the conjunction between blob paths and PSP's orbit for further study.

3.3. Multiscale In Situ Analysis of High-density Jets

We investigate the in situ measurements on April 29, when PSP crosses the blobs' paths (Figures 6(a)–(h)). During this period, PSP records two complete HCS crossings (00:54–01:52 and 08:14–08:51, diagnosed by polarity reversals in B_r and e-PAD) and one partial HCS crossing (09:24–10:21, diagnosed by half-reversed B_r and e-PAD), as shown in Figures 6(b)–(c). These HCS crossings span 2°∼4° in longitudes in Carrington coordinates, corresponding to 0.5∼1 $R_\odot$ at PSP's perihelion (∼16$R_\odot$ from the Sun). HCS crossings feature sharp B shears at both edges, indicating bifurcated structures. Bounded by the bifurcated current sheets, we find magnetic reconnection exhaust regions characterized by drops in total magnetic field strength ($|B|$) and enhancements in V_r (Figures 6(c)–(d)).

We further find HDJs coincide with these reconnection exhausts (blue shaded regions in Figure 6), featuring high N_p, N_e, and V_r. The velocity enhancement in HDJs ranges from 40 to 150 km s^{-1} while the Alfvén speed is around 120 km s^{-1} (based on the total magnetic field $|B| = 300$ nT and the proton number density $N_p = 3 \times 10^3$ cm^{-3}). We further calculate the proton and electron thermal pressures $p_{p/e,\mathrm{th}} = N_{p/e}\kappa T_{p/e}$, where κ is the thermal conductivity; the magnetic pressure $p_{\mathrm{mag}} = \frac{|B|^2}{2\mu_0}$ and the total pressure $p_{\mathrm{total}} = p_{p,\mathrm{th}} + p_{e,\mathrm{th}} + p_{\mathrm{mag}}$ (Figure 6(h)). The ratio between proton/electron thermal pressure and magnetic pressure ($\beta_{p/e} = p_{p/e,\mathrm{th}}/p_{\mathrm{mag}}$) is higher

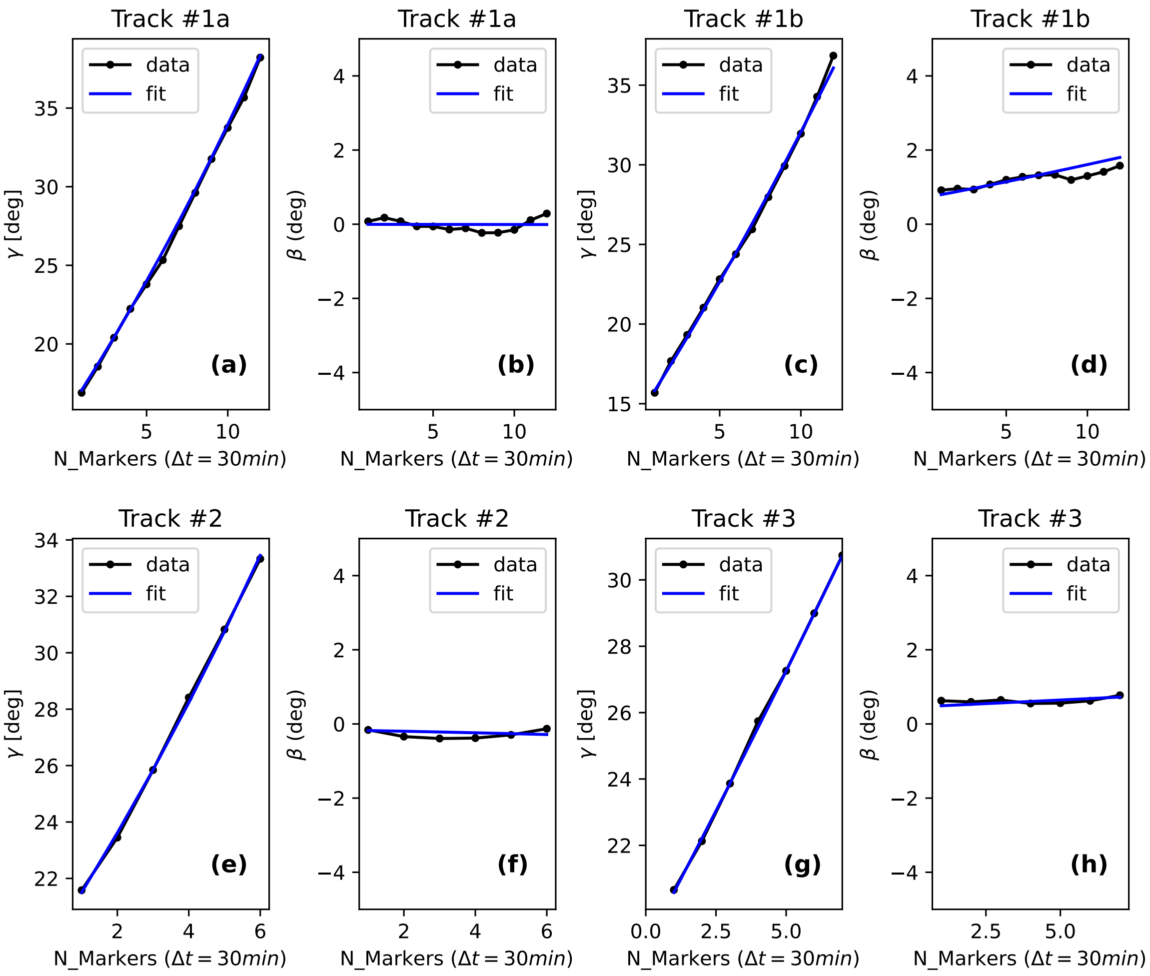

Figure 3. Trajectory fitting results. For each track, the left panel shows the original data and fitting result of the in-plane angle $\gamma(t)$, defined as the angle between the Sun, PSP, and the target's projection onto PSP's orbital plane. The right panel presents the corresponding out-of-plane angle $\beta(t)$, defined as the angle between the target, PSP, and the target's projection onto the orbital plane. The x-axis indicates the frame number in the running-difference image series, with a time cadence of 30 minutes per frame.

Table 1
Fitting Parameters of Four Blob Tracks

Track	r_0 ($R_\odot$)	v_r (km s^{-1})	ϕ_0 (deg)	δ_0 (deg)
Track #1a	9.14	282.77	30.67	−0.035
Track #1b	8.20	288.29	39.96	−0.09
Track #2	11.36	296.49	21.03	−0.02
Track #3	8.84	241.51	64.93	−0.085

inside HDJs (Figure 6(g)), which is commonly observed in streamer belts (J. Huang et al. 2023).

The approximate sizes, derived by multiplying the crossing time and the relative V_r between PSP and the solar wind in the radial direction, are 1.55, 0.90, and 1.45 $R_\odot$, compatible with the blob sizes estimated from WISPR images. Analogously, sizes in the normal direction (thickness of the HDJs) are 0.27 $R_\odot$ (1.9×10^5 km), 0.14 $R_\odot$ (1.0×10^5 km), and 0.21 $R_\odot$ (1.5×10^5 km), comparable to the thickness of remotely observed current sheets (J. Lin et al. 2005, 2007).

Encountered as PSP traverses the blob paths, the dense, fast HDJs align with the bright, fast blobs observed in WISPR. Thus, we propose that the blobs and HDJs are optical and in situ counterparts of recurrent reconnection jets in the HCS. They represent the same structure and process in the intermittently heated and accelerated SSW. Critical parameters of the blobs and HDJs are compared in Table 2. The estimated Carrington longitudes of intersections of blobs and PSP's orbit are also listed in Table 2, indicating one-to-one connections between HDJ 1 and Blob 2, HDJ 2 and Blob 1a, and HDJ 3 and Blob 1b.

To better understand the kinetic features of HDJs, we examine and compare proton VDFs inside and outside HDJs (Figures 6(j)–(o)). In the ambient SSW, proton VDFs exhibit

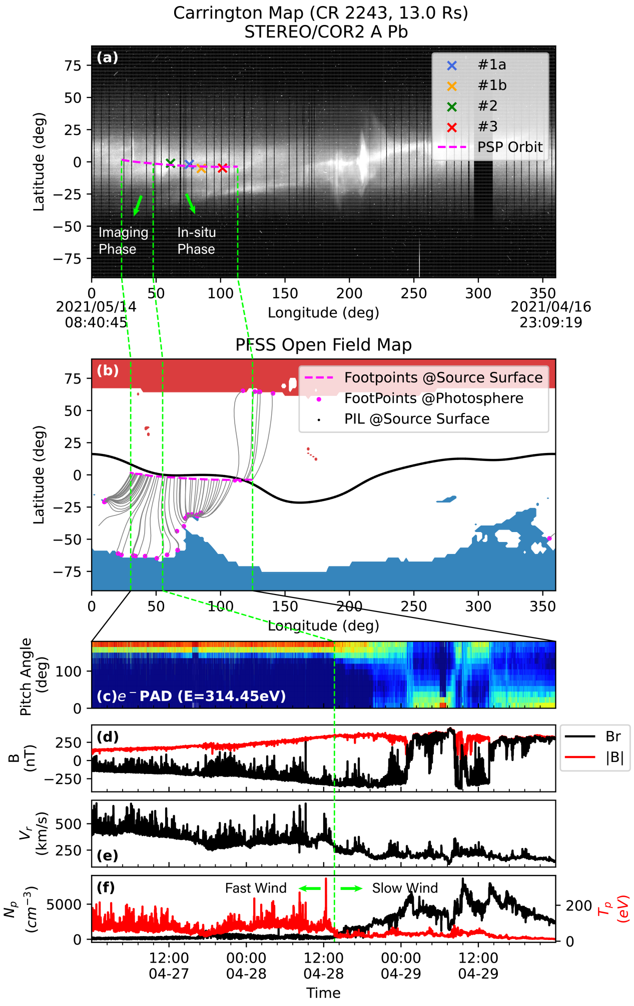

Figure 4. Macroscopic overview of PSP Encounter 8. (a) PSP's orbit and the projected positions of blobs on the white-light Carrington map. The magenta dashed line indicates the projection of PSP's trajectory, and the crosses mark the positions of blobs at 16 $R_\odot$. The three green dashed lines (from left to right in all panels) correspond to 00:00 UT on April 27, 13:40 UT on April 28, and 00:00 UT on April 30, respectively. (b) Magnetic connectivity map. The background shows the open magnetic field distribution calculated using the PFSS model. Red (blue) regions represent open fields of positive (negative) polarity. The black curve indicates the polarity inversion line at the source surface. The magenta dashed line traces PSP's footpoints on the source surface, and the dots represent corresponding footpoints on the photosphere. Gray curves show magnetic field lines connecting the photosphere and source surface. (c) Suprathermal electron pitch-angle distributions (e-PAD). (d) Radial magnetic field component B_r (black) and total magnetic field strength $|B|$ (red). (e) Radial bulk solar wind speed V_r. (f) Proton number density N_p (black) and proton temperature T_p (red). The green dashed line separates the measurements into two distinct phases.

"core + beam" patterns, suggesting that the young SSW is in a thermal nonequilibrium state (Figures 6(j), (l), and (n)). Inside HDJs, the proton VDFs are more bi-Maxwellian, and we can hardly resolve the beam components. Also, the velocity of the core component is higher inside HDJs than in the ambient SSW, and close to that of the beam component in HDJs. This suggests that the proton core is preferentially accelerated within the reconnection current sheet and therefore mixes with the beam component, leading to one bi-Maxwellian distribution. Similar cases are also noted by our recent work in the solar wind reconnection exhausts observed by Solar Orbiter (Z. Wu et al. 2023).

We further investigate small-scale structures inside HDJs, including filamentary current sheets, secondary magnetic reconnection jets, and flux ropes. A subset of these structures in HDJ-1 is shown in Figure 7. We also find structures with B_r and V_r positively correlated, $|B|$ and N_p negatively correlated, indicating possible involvement of slow-mode waves (Figures 7(i) and (j)). Current sheets with large magnetic shear angles are typically associated with magnetic reconnection (as shown in Figures 7(e), (f), and (g)) and appear at HDJ boundaries, specifically, in the bifurcated current sheet at the edges of primary magnetic reconnection exhausts. At these boundaries, internal magnetic field lines reconnect with external open field lines, allowing ambient SW material to enter the HDJs.

We also observe small-scale flux rope events, featuring a $|B|$ enhancement and magnetic field rotation (Figures 7(h) and (k)). These flux ropes are not isolated but embedded in current sheets, suggesting they result from local secondary reconnection. We identify an ongoing coalescence of two nascent flux ropes, causing component reconnection. Such merging flux ropes have been observed in magnetotail current sheets at Earth (R. Wang et al. 2016; J. A. Slavin et al. 2003) as well as in the near-Sun HCS (T. Phan et al. 2024). This finding indicates that HCS magnetic energy dissipation is not spatially isolated but occurs throughout the region, generating multiple small-scale flux ropes. This cascade-like process facilitates rapid magnetic energy dissipation and contributes to the heating and acceleration of SSW (J. F. Drake et al. 2006; C. Dong et al. 2022).

To study the orientation of the magnetic field fluctuations associated with the filamentary current sheets statistically, we perform a singular value decomposition analysis on the magnetic field time series of each HDJ. The eigenvector $\boldsymbol{k}$ with the minimum eigenvalue represents the direction of the current in secondary current sheets, normal to the filaments. We analyze the $\boldsymbol{k}$ distribution in the HDJ's LMN coordinates derived by minimum variance analysis (Figure 8). In the classic 2D tearing reconnection scenario, current filaments align with the current direction $\hat{e}_M$ of the primary current sheet. However, the orientation of current filaments in HDJs deviates from the $\hat{e_M}$ direction and appears randomly distributed. This suggests that the intermittent internal features of HDJs likely result from oblique tearing modes, which trigger turbulent reconnection in the primary current sheet and create filamentary current sheets deviating from the planar geometry, as found in simulations (W. Daughton et al. 2011) and in observations near Earth (R. Wang et al. 2023).

4. Discussion and Conclusion

In this study, we propose a novel "see and touch" technique and use it to integrate PSP's remote-sensing and in situ measurements of the young solar wind (Figure 9). We reveal that multiscale turbulent reconnection in the filamentary current sheets above streamers contributes to the heating and acceleration of young SSW. As the "eyes" of PSP, WISPR records ellipsoid plasma structures streaming out along streamer rays (Figure 9(a)). After "seeing" these blobs, PSP flies through their paths and "touches" HDJs as their counterparts (Figure 9(b)).

To exploit WISPR's constantly changing perspective due to PSP's motion, we use the "MEO-MISOF" algorithm to

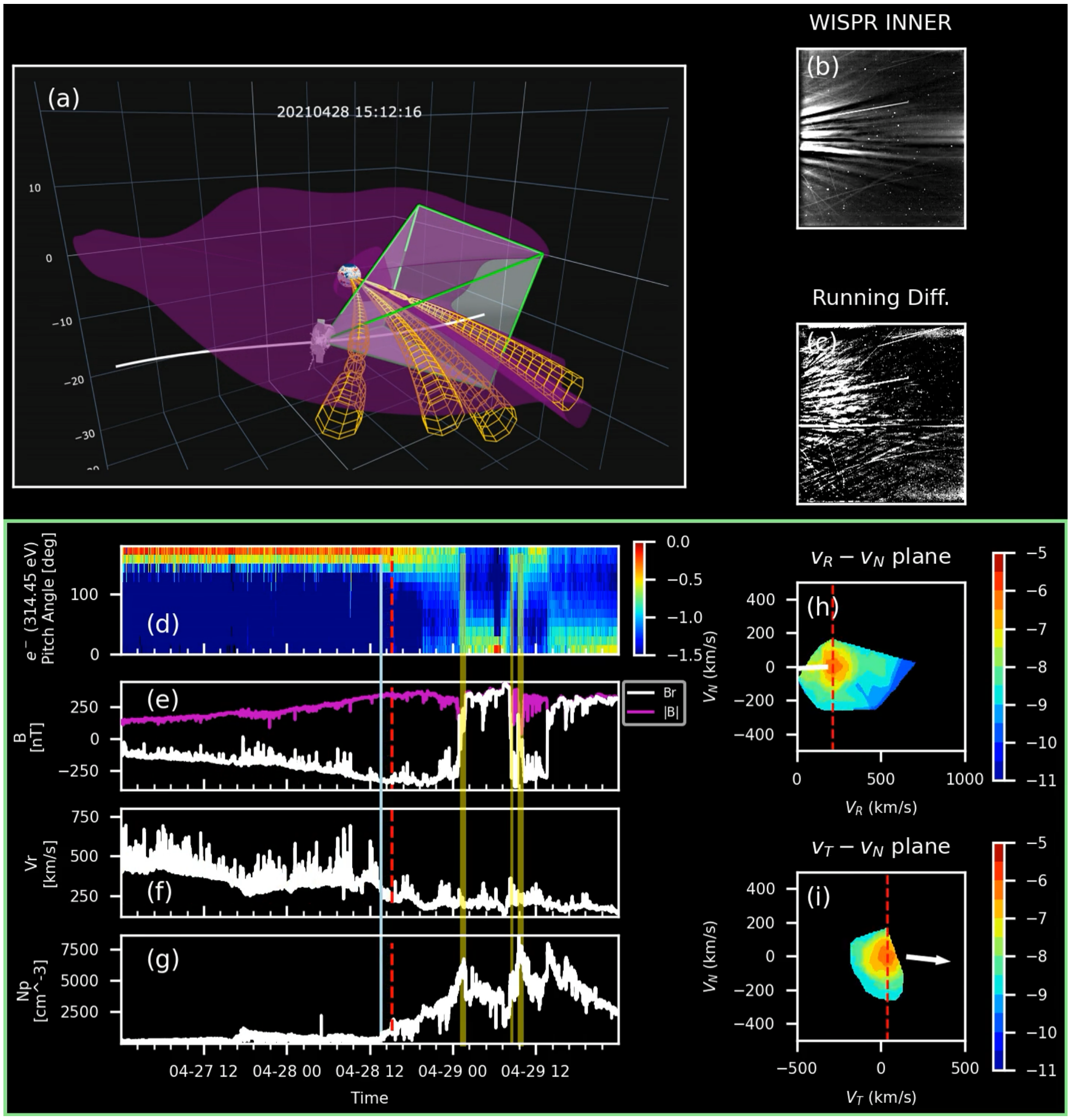

Figure 5. Illustration of the "see and touch" technique and PSP's observations. (a) The central sphere represents the Sun (not to scale), colored by the radial magnetic field component B_r. The purple surface represents HCS as the isosurface where $B_r = 0$. These elements are plotted based on simulation data from PSI. Yellow tubes represent flux tubes corresponding to blobs/HDJs, constructed along the fitted trajectories of blobs and are pinched to illustrate magnetic reconnection-driven blob formation. PSP's orbit is shown as a white curve, and the WISPR field of view is outlined in green. (b)–(c) The original and running-difference WISPR images. (d)–(g) The in situ measurements, including pitch angle distribution of suprathermal electrons (e-PAD), total and radial magnetic field components ($|B|$ and B_r), solar wind radial bulk velocity (V_r), and solar wind number density (N_p). The light blue line marks 13:40 UT on April 30, before which we focus on PSP's white-light images and after on the in situ measurements. The light yellow shades mark the HDJs measured in situ. (h)–(i) The slices of the proton VDF (the radial–normal plane and the tangential–normal plane). The white arrow shows the projected magnitude and direction of the magnetic field. The red dashed lines show the positions with the maximum phase density. The animation spans from April 27 00:00 to April 29 23:59, showing PSP's observations alongside its position and camera field of view relative to the HCS and blob trajectories. In panels (d)–(g), red dashed lines mark the current in situ measurements by PSP, while the green frame highlights the specific measurements central to our "see and touch" analysis.

(An animation of this figure is available in the online article.)

reconstruct the 3D trajectories of these blobs. We find that the recurrent blobs are formed close to the Sun and then move along the streamer at a speed of 240–290 km s^{-1}. T. D. Phan et al. (2020) calculated the distance between PSP and the reconnection X-lines during Encounter 1 and suggested that the reconnection exhausts are formed close to the spacecraft. However, this result is limited by the asymmetric nature of reconnection exhausts observed in situ. Further observation and modeling work is required to address this problem. Although we assume uniform motion while fitting the remote-sensing observations of the blobs, this assumption does not contradict the acceleration phenomena observed in situ within reconnection exhaust regions. The ambient solar wind outside the blob moves slower than the plasma inside. As the ambient solar wind material enters the reconnection exhaust region through the reconnection inflow, it is accelerated to match the overall flow speed of the original material inside the blob.

While deciding the source regions of the solar wind (Figure 4), the boundary between fast wind and slow wind (around April 28, 13:00) does not fully coincide with the shift

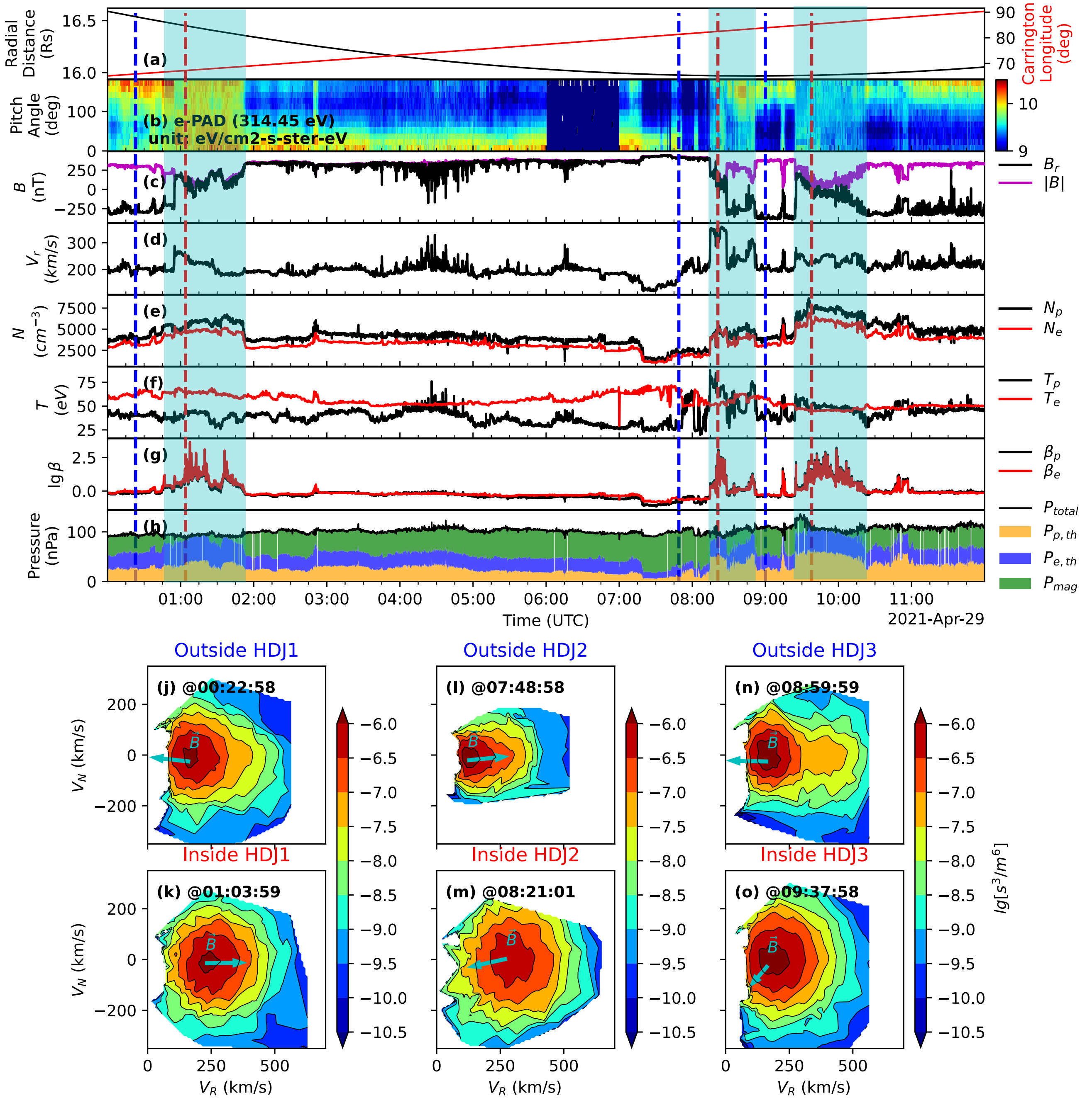

Figure 6. Comprehensive analysis of HDJs and the surrounding plasma environment. (a) Radial distance and Carrington longitude of PSP. (b) Pitch-angle distribution of suprathermal electrons (e-PAD) at 314.45 eV. (c) Radial magnetic field component B_r (black) and total magnetic field strength $|B|$ (purple). (d) Radial solar wind velocity V_r. (e) Proton number density N_p (black) and electron number density N_e (red). (f) Proton temperature T_p (black) and electron temperature T_e (red). (g) Ratio between thermal and magnetic pressure of protons β_p (black) and electrons β_e (red). (h) Pressure components: proton thermal pressure $P_{p,\mathrm{th}}$ (yellow), electron thermal pressure $P_{e,\mathrm{th}}$ (blue), magnetic pressure P_{mag} (green), and total pressure P_{total} (black). Three HDJ intervals are highlighted by light blue shaded regions. (j)–(o) Proton velocity distribution function (VDF) slices in the V_R–V_N plane at selected timestamps, indicated by red dashed lines in the upper panels. Each VDF slice corresponds to a characteristic time outside (upper rows) or inside (lower rows) the HDJ intervals.

in footpoints from polar coronal holes to equatorial coronal holes. This discrepancy does not affect our results because we mainly focus on the source regions of the in situ measured slow wind (from April 29, 00:00 to 12:00). However, this misalignment likely stems from uncertainties in the two-step ballistic mapping method. This mapping approach has been widely used to explore magnetic connectivity between the Sun and spacecraft such as PSP (S. D. Bale et al. 2023; C. Hou et al. 2024). The uncertainty typically arises from three factors: the selection of the source surface height for the PFSS model, solar wind acceleration, and solar rotation (A. R. Macneil et al. 2022; A. Koukras et al. 2025). The resulting positional error is usually less than 10° (S. D. Bale et al. 2023; C. Hou et al. 2024). In our study, we implement the same approach as C. Hou et al. (2024), using time-dependent magnetograms (1 hr time resolution) and solar wind propagation time calculated from PSP's radial distance and measured solar wind velocity to minimize the error.

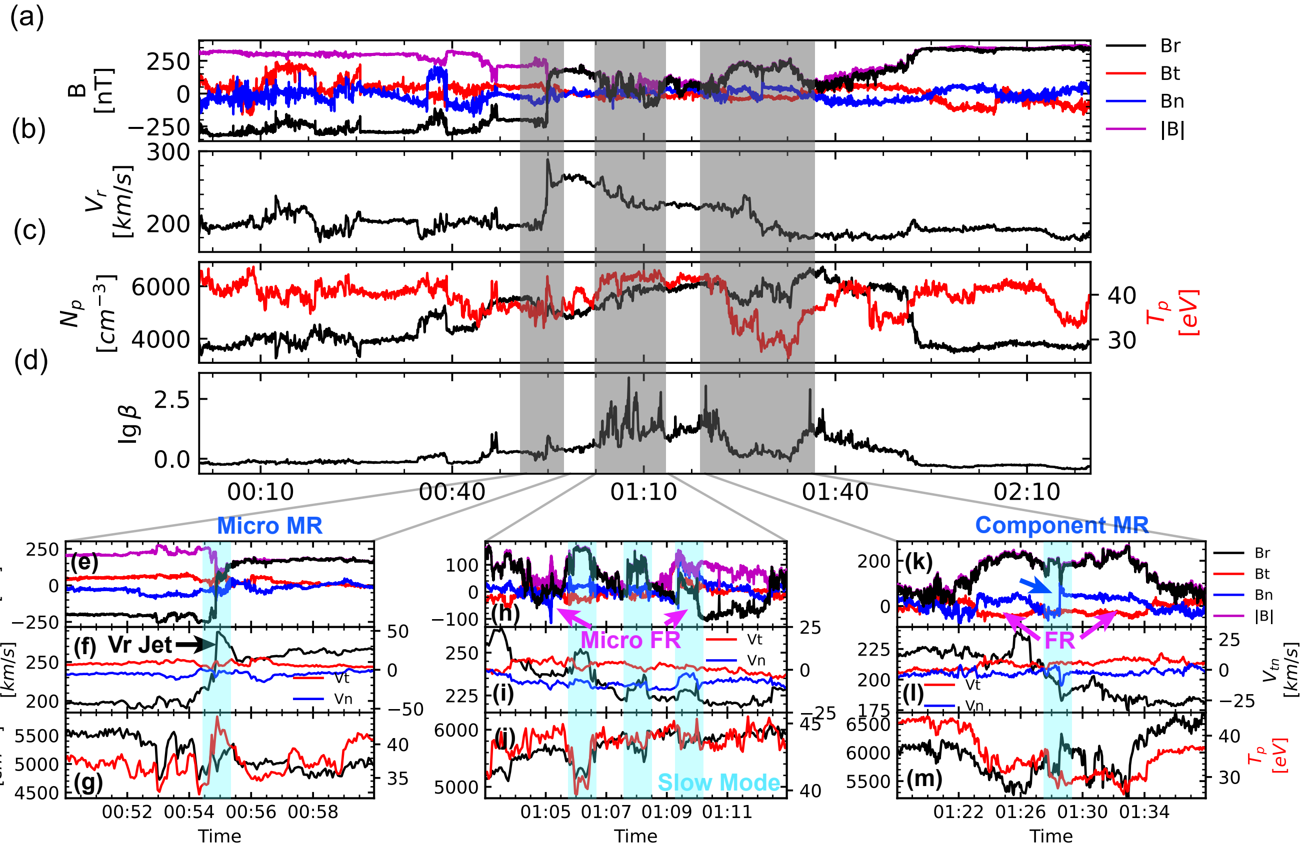

Figure 7. Detailed examination of HDJ-1. (a)–(d) Overview of plasma and magnetic field properties during HDJ-1. (a) Magnetic field strength $|B|$ and the components B_r, B_t, and B_n. The green line shows the modeled magnetic field profile corresponding to a tearing-unstable current sheet. (b) Radial proton bulk velocity V_r. (c) Proton number density N_p and temperature T_p. (d) β_p. (e)–(m) Zoomed-in views of substructures within HDJ-1, corresponding to the gray-shaded intervals in panels (a)–(d). First row: $|B|$, B_r, B_t, and B_n. Second row: V_r, V_t, and V_n. Third row: N_p and T_p.

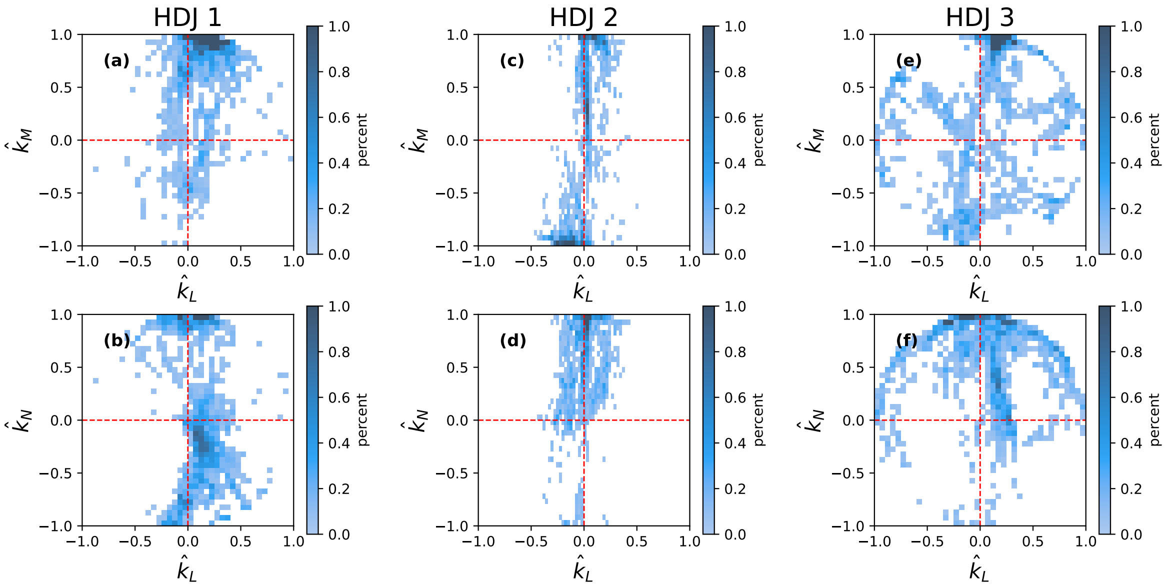

Figure 8. Distribution of the unit wavevector $\hat{k}$ in HDJs, expressed in LMN coordinates. The vector $\hat{k}$ denotes the direction of the eigenvector corresponding to the smallest eigenvalue obtained from the singular value decomposition of the magnetic field time series $\boldsymbol{B}$. This analysis targets 10 s scale structures within each HDJ, which correspond to spatial scales of approximately 1000 ion inertial lengths, based on average plasma parameters. The LMN coordinate system for each HDJ is determined individually via minimum variance analysis.

With a detailed analysis of in situ measurements, we find that the core component of the proton VDF is preferentially heated and accelerated to a similar velocity as the beam component after entering the reconnection exhaust (HDJ/blobs), leading to a bi-Maxwellian distribution. This represents the kinetic physics in the reconnection exhaust regions (blobs/

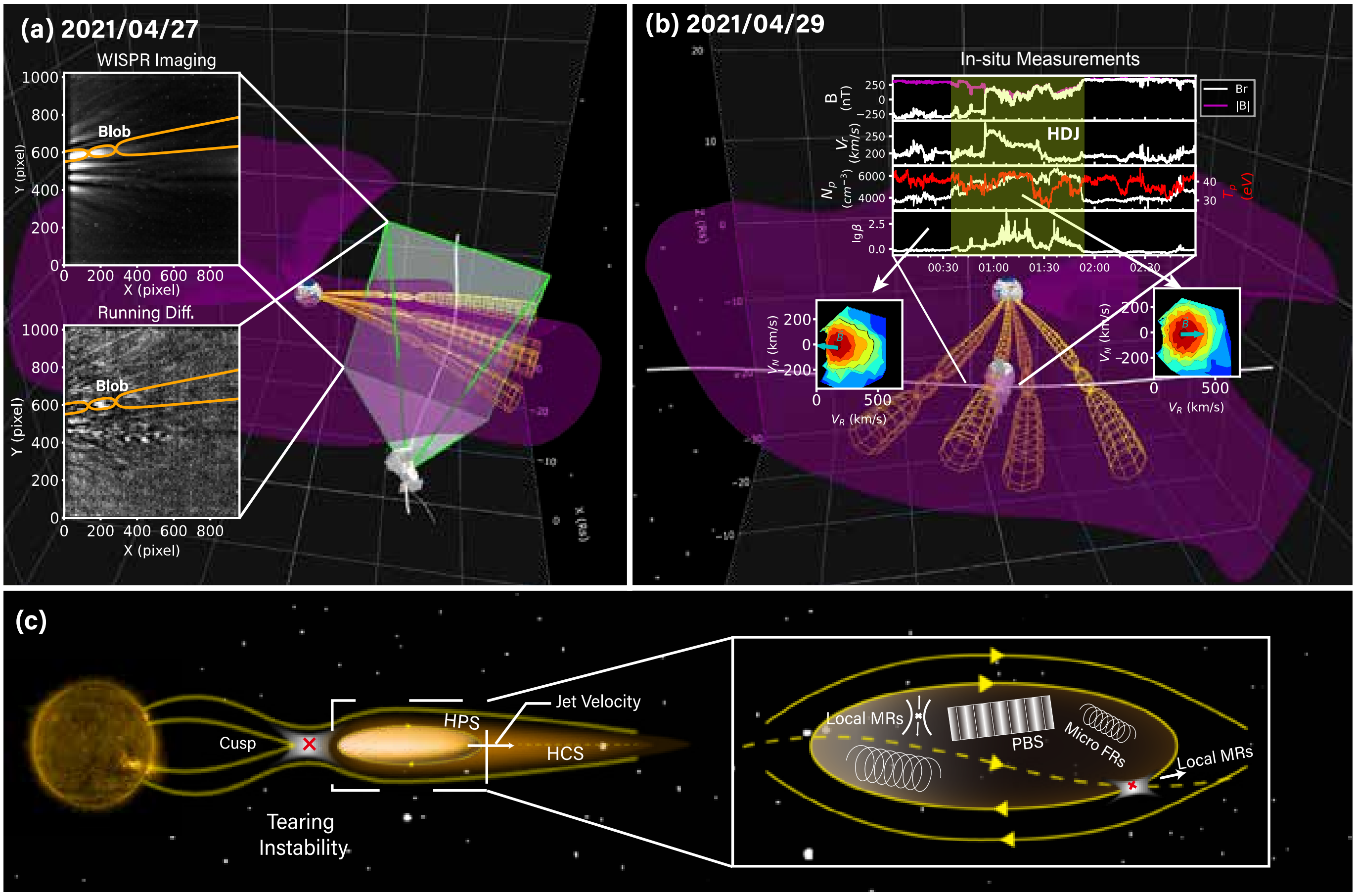

Figure 9. Illustration of the "see and touch" technique and the multiscale structure of a streamer blob. Elements in (a)–(b): The central sphere represents the Sun (not to scale), colored by the radial magnetic field component B_r. The purple surface represents the HCS as the isosurface where $B_r = 0$. These elements are plotted based on CORHEL simulation data from Predictive Science Inc. (PSI). Yellow tubes represent flux tubes corresponding to blobs/HDJs, constructed along the fitted trajectories of blobs and are pinched to illustrate magnetic-reconnection-driven blob formation. PSP's orbit is shown as a white curve, and the WISPR field of view is outlined in green. (a) On 2021 April 27, PSP remotely observed streamer blobs using WISPR. Subpanels display both original and running-difference images of the blobs. (b) On 2021 April 29, PSP encounters the same set of blobs in situ. Subpanels display in situ measurements (from top to bottom: $|B|$ and B_r, V_r, N_p and T_p, and β_p) and proton VDFs during the crossing. (c) Conceptual sketch of the multiscale structure within a streamer blob: large-scale magnetic islands generated by tearing-mode reconnection, and small-scale kinetic structures generated by turbulence within the blob.

Table 2
Comparison between Blobs Observed in Remote Sensing and HDJs Measured In Situ

Structure	Carr. Long. (deg)	Length ($R_\odot$)	Width ($R_\odot$)	$N_p r^2$ Peak (Ambient) (10^6 cm^{-3} $R_\odot^2$)	Velocity (km s^{-1})	Counterpart
HDJ 1	66.90	1.55	0.27	~1.6 (1.0)	~260	Blob 2
HDJ 2	82.70	0.90	0.14	~1.2 (0.6)	~300–340	Blob 1a
HDJ 3	84.70	1.45	0.21	~2.0 (1.0)	~250	Blob 1b
Blob 1a	76.0	~1.2 (at 11 $R_\odot$), ~1.7 (at 17 $R_\odot$)	0.3–0.5	Brighter than background	283	HDJ 2
Blob 1b	84.5	~1.2 (at 11 $R_\odot$), ~1.7 (at 17 $R_\odot$)	0.3–0.5	Brighter than background	288	HDJ 3
Blob 2	62.5	~1.2 (at 11 $R_\odot$), ~1.7 (at 17 $R_\odot$)	0.3–0.5	Brighter than background	296	HDJ 1
Blob 3	101.5	~1.2 (at 11 $R_\odot$), ~1.7 (at 17 $R_\odot$)	0.3–0.5	Brighter than background	242	...

HDJs). Additionally, we identify multiple secondary reconnection events at the boundary and inside the HDJs and their byproducts (small-scale jets and flux ropes). The presence of small-scale structures indicates that turbulence forms filamentary current sheets inside HDJs, triggering turbulent reconnection that facilitates more efficient heating and acceleration of young SSW. Further analysis based on modeling is required to reveal the trigger mechanisms of reconnection.

The "see and touch" technique exploits PSP's unique orbit to combine remote-sensing and in situ measurements. It is particularly suitable for studying multiscale structures and processes in the pristine solar wind. This technique has enormous potential in other PSP encounters and future near-Sun missions.

Acknowledgments

The authors acknowledge the contributions of the Parker Solar Probe mission operations and spacecraft engineering teams at the Johns Hopkins University Applied Physics Laboratory and the FIELDS, SWEAP, and WISPR teams for providing the data. We would also like to acknowledge the data provided by GONG, STEREO, and Predictive Science Inc. (PSI). We thank Lami Chan and Zheng Sun for inspiring discussions and continuous encouragement. The authors from China are supported by NSFC, NKRDC, and CNSA under the following grant Nos. 42241118, 42530105, 42174194, 2021YFA0718600, 2022YFF0503800, 42150105, 42204166, D050106, and D050103. C.H. is supported by the Alexander von Humboldt Foundation. A.R. is funded by the ERC SLOW SOURCE project (DLV-819189). D.V. is supported by STFC Consolidated Grant ST/W001004/1.

ORCID iDs

Ziqi Wu https://orcid.org/0000-0002-1349-8720
Jiansen He https://orcid.org/0000-0001-8179-417X
Chuanpeng Hou https://orcid.org/0000-0001-7205-2449
Die Duan https://orcid.org/0000-0002-6300-6800
Jia Huang https://orcid.org/0000-0002-9954-4707
Alexis P. Rouillard https://orcid.org/0000-0003-4039-5767
Daniel Verscharen https://orcid.org/0000-0002-0497-1096
Yao Chen https://orcid.org/0000-0001-6449-8838
Rui Zhuo https://orcid.org/0000-0003-4726-9755
Tianhang Chen https://orcid.org/0000-0001-7170-0408

References

Abbo, L., Ofman, L., Antiochos, S. K., et al. 2016, SSRv, 201, 55
Annex, A., Pearson, B., Seignovert, B., et al. 2020, JOSS, 5, 2050
Antiochos, S., Mikić, Z., Titov, V., Lionello, R., & Linker, J. 2011, ApJ, 731, 112
Badman, S. T., Bale, S. D., Martínez Oliveros, J. C., et al. 2020, ApJS, 246, 23
Bale, S. D., Drake, J. F., McManus, M. D., et al. 2023, Natur, 618, 252
Bale, S. D., Goetz, K., Harvey, P. R., et al. 2016, SSRv, 204, 49
Chen, Y., Li, X., Song, H. Q., et al. 2009, ApJ, 691, 1936
Chitta, L. P., Huang, Z., D'Amicis, R., et al. 2025, A&A, 694, A71
Cranmer, S. R., Asgari-Targhi, M., Miralles, M. P., et al. 2015, RSPTA, 373, 20140148
Daughton, W., Roytershteyn, V., Karimabadi, H., et al. 2011, NatPh, 7, 539
Dong, C., Wang, L., Huang, Y.-M., et al. 2022, SciA, 8, eabn7627
Drake, J. F., Swisdak, M., Che, H., & Shay, M. A. 2006, Natur, 443, 553
Eriksson, S., Swisdak, M., Mallet, A., et al. 2024, ApJ, 965, 76
Feldman, U., Landi, E., & Schwadron, N. A. 2005, JGRA, 110, A07109
Fox, N. J., Velli, M. C., Bale, S. D., et al. 2016, SSRv, 204, 7
He, J.-S., Tu, C.-Y., & Marsch, E. 2008, SoPh, 250, 147
Hou, C., He, J., Duan, D., et al. 2024, NatAs, 8, 1246
Howard, R. A., Moses, J. D., Vourlidas, A., et al. 2008, SSRv, 136, 67
Huang, J., Kasper, J. C., Larson, D. E., et al. 2023, ApJS, 265, 47
Kasper, J. C., Abiad, R., Austin, G., et al. 2016, SSRv, 204, 131
Koukras, A., Dolla, L., & Keppens, R. 2025, A&A, 694, A134
Lapenta, G., & Knoll, D. A. 2005, ApJ, 624, 1049
Lavraud, B., Fargette, N., Réville, V., et al. 2020, ApJL, 894, L19
Liewer, P., Vourlidas, A., Thernisien, A., et al. 2019, SoPh, 294, 93
Liewer, P. C., Qiu, J., Ark, F., et al. 2022, SoPh, 297, 128
Liewer, P. C., Qiu, J., Penteado, P., et al. 2020, SoPh, 295, 140
Liewer, P. C., Vourlidas, A., Stenborg, G., et al. 2023, ApJ, 948, 24
Lin, J., Ko, Y. K., Sui, L., et al. 2005, ApJ, 622, 1251
Lin, J., Li, J., Forbes, T. G., et al. 2007, ApJL, 658, L123
Linker, J. A., Mikić, Z., Biesecker, D. A., et al. 1999, JGR, 104, 9809
Livi, R., Larson, D. E., Kasper, J. C., et al. 2022, ApJ, 938, 138
Macneil, A. R., Owens, M. J., Finley, A. J., & Matt, S. P. 2022, MNRAS, 509, 2390
Martinović, M. M., Dordević, A. R., Klein, K. G., et al. 2022, JGRA, 127, e30182
Matsumoto, T., & Suzuki, T. K. 2014, MNRAS, 440, 971
McComas, D., Bame, S., Barraclough, B., et al. 1998, GeoRL, 25, 1
Owens, M. J., Crooker, N., & Lockwood, M. 2014, JGRA, 119, 36
Phan, T., Drake, J., Larson, D., et al. 2024, ApJL, 971, L42
Phan, T. D., Bale, S. D., Eastwood, J. P., et al. 2020, ApJS, 246, 34
Phan, T. D., Verniero, J. L., Larson, D., et al. 2022, GeoRL, 49, e96986
Pulupa, M., Bale, S. D., Bonnell, J. W., et al. 2017, JGRA, 122, 2836
Réville, V., Fargette, N., Rouillard, A. P., et al. 2022, A&A, 659, A110
Riley, P., Linker, J., & Mikić, Z. 2002, JGRA, 107, 1136
Riley, P., Linker, J. A., Lionello, R., & Mikic, Z. 2012, JASTP, 83, 1
Rouillard, A. P., Davies, J. A., Lavraud, B., et al. 2010, JGRA, 115, A04103
Rouillard, A. P., Kouloumvakos, A., Vourlidas, A., et al. 2020, ApJS, 246, 37
Sanchez-Diaz, E., Rouillard, A. P., Davies, J. A., et al. 2017, ApJL, 835, L7
Sanchez-Diaz, E., Rouillard, A. P., Lavraud, B., Kilpua, E., & Davies, J. A. 2019, ApJ, 882, 51
Sheeley, N. R., Walters, J. H., Wang, Y. M., & Howard, R. A. 1999, JGR, 104, 24739
Sheeley, N. R., Wang, Y. M., Hawley, S. H., et al. 1997, ApJ, 484, 472
Sheeley, N. R. J., Herbst, A. D., Palatchi, C. A., et al. 2008, ApJ, 675, 853
Sheeley, N. R. J., Knudson, T. N., & Wang, Y. M. 2001, ApJL, 546, L131
Sheeley, N. R. J., & Wang, Y. M. 2014, ApJ, 797, 10
Shi, C., Velli, M., Bale, S. D., et al. 2022, PhPl, 29, 122901
Shoda, M., Suzuki, T. K., Asgari-Targhi, M., & Yokoyama, T. 2019, ApJL, 880, L2
Slavin, J. A., Lepping, R. P., Gjerloev, J., et al. 2003, JGRA, 108, 1015
Song, H. Q., Chen, Y., Liu, K., Feng, S. W., & Xia, L. D. 2009, SoPh, 258, 129
Telloni, D., Zank, G. P., Sorriso-Valvo, L., et al. 2022, ApJ, 935, 112
Viall, N. M., DeForest, C. E., & Kepko, L. 2021, FrASS, 8, 139
Vourlidas, A., Howard, R. A., Plunkett, S. P., et al. 2016, SSRv, 204, 83
Wang, R., Lu, Q., Nakamura, R., et al. 2016, NatPh, 12, 263
Wang, R., Wang, S., Lu, Q., et al. 2023, NatAs, 7, 18
Wang, Y. M., Sheeley, N. R., Socker, D. G., Howard, R. A., & Rich, N. B. 2000, JGR, 105, 25133
Wang, Y. M., Sheeley, N. R. J., Walters, J. H., et al. 1998, ApJL, 498, L165
Whittlesey, P. L., Larson, D. E., Kasper, J. C., et al. 2020, ApJS, 246, 74
Wu, Z., He, J., Duan, D., et al. 2023, ApJ, 951, 98